Supplement of Hydrol. Earth Syst. Sci., 22, 4061–4082, 2018
https://doi.org/10.5194/hess-22-4061-2018-supplement

Hydrology and Earth System Sciences
Open Access
EGU

Supplement of

Understanding terrestrial water storage variations in northern latitudes across scales

Tina Trautmann et al.

Correspondence to: Tina Trautmann (ttraut@bgc-jena.mpg.de)

Supplement

S1 Detailed model description and formulas

The model consists of three components: (1) a snow component that simulates accumulation and ablation of snow, (2) a soil water component to calculate soil moisture, evapotranspiration and land runoff, and (3) a runoff component that derives total runoff. All modelled fluxes and states correspond to the spatio-temporal resolution of the forcing data, which in this study is a 1° x 1° latitude/longitude grid and daily time steps.

The following describes all implemented processes and equations in detail.

S1.1 Snow Component

Snow storage is implemented as a simple accumulation and melt approach, which further is extended by consideration of sublimation and fractional snow cover. The snow storage as described by the snow water equivalent SWE [mm] at time t [d] is calculated as mass balance:

$$\mathbf{SWE_t = SWE_{t-1} + SF_t - ETSub_t - M_t} \quad \text{(S1)}$$

where SWE_{t-1} [mm] is the snow water equivalent of the preceding time step which is increased by snowfall SF_t [mm d^{-1}] and reduced by the amount of sublimation $ETSub_t$ [mm d^{-1}] and snow melt M_t [mm d^{-1}].

All precipitation P [mm d^{-1}] is assumed to fall as snow at temperatures below 0 °C. Since precipitation estimates, especially during the cold season, are known for biases due to substantial under-catch (Rudolf and Rubel, 2005;Seo et al., 2010), P is scaled using the parameter p_{sf} to derive SF at time t:

$$\mathbf{SF_t = p_{sf} \cdot P_t \quad | T < 0°C} \quad \text{(S2)}$$

In order to incorporate sub-grid variability, the fraction of the grid cell covered by snow is computed following the H-TESSEL approach (Balsamo et al., 2009;ECMWF, 2014):

$$\mathbf{FSC_t = \min\left(\frac{SWE_{t-1}}{sn_c}, 1\right)} \quad \text{(S3)}$$

with fractional snow cover FSC [-] at time t being linearly dependent on SWE_{t-1} of the preceding time step and the parameter sn_c [mm] being the minimum SWE that ensures complete snow coverage of the grid cell.

Further, snow melt M and sublimation ETSub are assumed to only emerge from snow covered area by using FSC as scaling factor in the calculation of these fluxes.

Snow melt M occurs when snow storage is present and temperature exceeds melting temperature. Based on the restricted degree-day radiation balance approach described by Kustas et al. (1994), melt M [mm d^{-1}] at time t depends on temperature T_t [°C] and net radiation Rn_t [MJ m^{-2} d^{-1}]:

$$\mathbf{M_t} = (\mathbf{m_t} \cdot \mathbf{T_t} + \mathbf{m_r} \cdot \mathbf{Rn_t}) \cdot \mathbf{FSC_t} \quad | \mathbf{T > 0°C} \tag{S4}$$

where the degree-day factor m_t [mm $°C^{-1}$] and the radiation factor m_r [mm MJ^{-1}] control the melt rate.

The derivation of snow sublimation ETSub is adapted from the approach implemented in the GLEAM model. This technique is based on the Priestley and Taylor (1972) formula, which calculates evaporation rate as latent heat flux LE [MJ m^{-2} d^{-1}] based on the available energy Rn [MJ m^{-2} d^{-1}], ground heat flux G [MJ m^{-2} d^{-1}]) and a dimensionless coefficient sn_a that parameterizes evaporation-resistance. LE at time t is derived by

$$\mathbf{LE_t} = \left(\mathbf{sn_a} \cdot \frac{\mathbf{\Delta sn_t}}{\mathbf{\Delta sn_t + \gamma sn_t}} \cdot (\mathbf{Rn_t - G})\right) \cdot \mathbf{FSC_t} \tag{S5}$$

with Δsn_t being the slope of the temperature/saturated vapor pressure curve [kPa K^{-1}] and γsn_t representing the psychrometric constant [kPa K^{-1}]. Both, Δsn and γsn, are modified for snow covered areas according to Murphy and Koop (2005).
They calculate Δsn_t as a function of T_t [K] (Eq.(S6)), and γsn_t as a function of atmospheric pressure Pair [kPa], specific heat of air at constant pressure c_p [MJ kg^{-1} K^{-1}], the ratio molecular weight of water vapor/dry air MW and latent heat of sublimation of ice λsn [MJ kg^{-1}] (Eq.(S7)).

$$\mathbf{\Delta sn_t} = \left(\frac{5723.265}{\mathbf{T_t^2}} + \frac{3.53069}{\mathbf{T_t - 0{,}00728332}}\right) \cdot \mathbf{e}^{9.550426 - \frac{5723.265}{T_t} + 3.53068 \cdot \ln(T_t) - 0{,}00728332 \cdot T_t} \tag{S6}$$

$$\mathbf{\gamma sn_t} = \frac{\mathbf{Pair} \cdot \mathbf{c_p}}{\mathbf{MA} \cdot \mathbf{\lambda sn_t}} \tag{S7}$$

In Eq.(S7), Pair is assumed to be time- and space-invariant with a uniform value of 101.3 kPa and c_p = 0.001 MJ kg^{-1} K^{-1}. MA is a constant of 0.622 and λsn is defined by Murphy and Koop (2005) as a function of T_t [K]. With a molecular mass of water of 18.01528 g mol^{-1}, λsn can be calculated as:

$$\lambda sn_t = \left(46782.5 + 35.8925 \cdot T_t - 0.07414 \cdot T_t^2 + 541.5 \cdot e^{-\left(\frac{T_t}{123.75}\right)^2}\right) \cdot \frac{0.001}{18.01528} \quad \text{(S8)}$$

Since snow-covered ecosystems can be assumed to be unstressed due to the sufficient availability of water, LE corresponds to actual sublimation ETSub (Miralles et al., 2011). And ETSub [mm d^{-1}] can be converted from LE through division by λsn:

$$ETSub_t = \frac{LE_t}{\lambda sn_t} \quad \text{(S9)}$$

Altogether, the model calculates ETSub as a function of T_t, Rn_t, Pair, G, sn_a and FSC_t. While T_t, Rn_t and FSC_t are variable in time and space and depend on input data, the approach postulates constant Pair = 101.3 kPa and G = 0 MJ m^{-2} d^{-1}.

S1.2 Soil component

The central part of the model is the soil water component, which distributes input from rain fall and snow melt to soil water storage SM [mm], actual evapotranspiration ET [mm d^{-1}] and land runoff Qs [mm d^{-1}].

Like snow, the calculation of soil water storage as represented by soil moisture SM [mm] at time t follows the mass balance

$$SM_t = SM_{t-1} + In_t - ET_t \quad \text{(S10)}$$

with SM_{t-1} [mm] being the soil moisture of the preceding time step which is increased by infiltration In_t [mm d^{-1}] and reduced by actual evapotranspiration ET_t [mm d^{-1}].

On the one hand, the amount of infiltration In [mm d^{-1}] depends on the possible inflow IW [mm d^{-1}], which is the sum of rain fall RF (precipitation P if T ≥ 0°C) and snow melt M at time t:

$$IW_t = RF_t + M_t \quad \text{(S11)}$$

On the other hand, a part of IW may not infiltrate due to current soil moisture conditions but contribute to (direct) land runoff Qs [mm d^{-1}]. To estimate the partitioning of IW into SM and Qs, Qs at time t is calculated after Bergström (1995) as:

$$Qs_t = IW_t \cdot \left(\frac{SM_{t-1}}{s\_max}\right)^{S_{exp}} \quad \text{(S12)}$$

In Eq.(S12) Qs_t depends on the inflow IW_t, the runoff coefficient s_{exp} and the actual soil moisture SM_{t-1} compared to its maximum water holding capacity s_{max}. Thus, no land runoff occurs if the soil water storage is empty and all IW is allocated to land runoff if the soil is completely saturated. Between these points, s_{exp} determines the amount of inflow that converts to Qs. While low values of s_{exp} lead to a high amount of Qs even if the soil moisture deficit is low (e.g. low SM/s_{max} ratio), higher values of s_{exp} increase the proportion of IW that infiltrates.

Infiltration In at time t is derived in accordance to the law of conservation of mass as:

$$\mathbf{In_t = IW_t - Qs_t} \tag{S13}$$

Potential evapotranspiration potET [mm d^{-1}] at time t is derived from net radiation Rn [MJ m^{-2} d^{-1}] and air temperature T [°C] according to the Priestley-Taylor formula (Priestley and Taylor, 1972), where et_a is the alpha coefficient:

$$\mathbf{potET_t = et_a \cdot \left(\frac{\Delta_t}{\Delta_t + \gamma_t} \cdot \frac{Rn_t}{\lambda_t}\right)} \tag{S14}$$

where Δ_t is the slope of the temperature/saturated vapor pressure curve [kPa K^{-1}], λ_t the latent heat of vaporization [MJ kg^{-1}] and γ_t the psychrometric constant [kPa K^{-1}].

The slope of the saturated vapor pressure curve Δ_t, as well as the latent heat of vaporization λ_t are functions of T at time t:

$$\mathbf{\Delta_t = \frac{4098 \cdot 0.611 \cdot e^{\frac{17.27 \cdot T_t}{T_t + 237.3}}}{(T_t \cdot 237.3)^2}} \tag{S15}$$

$$\mathbf{\lambda_t = 2.501 - (2.361 \cdot 10^{-3}) \cdot T_t} \tag{S16}$$

Analogue to Eq.(S7), γ_t depends on a constant atmospheric pressure Pair of 101.3 kPa, the specific heat of air at constant pressure c_p [MJ kg^{-1} K^{-1}], the constant MA and the latent heat of vaporization λ_t:

$$\mathbf{\gamma_t = \frac{Pair \cdot c_p}{MA \cdot \lambda_t}} \tag{S17}$$

In order to avoid complete depletion of the soil water storage and to account for cohesion of water in the soil matrix, only a fraction of soil moisture after infiltration is assumed to be available for evapotranspiration. We express the sensitivity of evapotranspiration to available water similar to Teuling et al. (2006) by the parameter et_{sup}. Thus, et_{sup} determines the portion

of the sum of infiltration In_t [mm d^{-1}] and soil moisture SM_{t-1} [mm], that represents evapotranspiration supply supET [mm d^{-1}] at time t:

$$\mathbf{supET_t = et_{sup} \cdot (SM_{t-1} + In_t)} \quad \text{(S18)}$$

Finally, actual evapotranspiration ET [mm d^{-1}] at time t is derived by comparing $potET_t$ [mm d^{-1}] and $supET_t$ [mm d^{-1}]:

$$\mathbf{actET_t = min(potET_t, supET_t)} \quad \text{(S19)}$$

S1.3 Runoff component

As total runoff comprises fast direct runoff as well as delayed interflow and base flow, it's appropriate to consider retardation (Orth et al., 2013). Accordingly, total runoff Q [mm d^{-1}] at time t results from the accumulated effects of all land runoff Qs [mm d^{-1}] generated during the preceding 60 time steps:

$$\mathbf{Q_t = \sum_{i=0}^{60} Qs_{t-i} \cdot \underbrace{\left[e^{-\frac{i}{q_t}} - e^{-\frac{i+1}{q_t}}\right]}_{\text{delay component}}} \quad \text{(S20)}$$

where the recession time scale q_t [d] determines how quickly land runoff is transformed into streamflow. In theory, an infinite number of time steps would be necessary to ensure that all generated Qs is transformed into Q. However, the arbitrary number of 60 days allows accounting for > 99 % of Qs (Orth et al., 2013), as long as q_t is below 13 days. To allow longer recession times when calibrating the model and still account for > 99 % of Qs within the 60 days-window, the delay component of Eq.(S20) is scaled with its sum.

Introducing temporal delay leads to retention of a portion of Qs, and thus to an additional, temporal storage of retained water RW [mm]. The change of retained water storage ΔRW [mm d^{-1}] at time t can be inferred using the water balance:

$$\mathbf{0 = P_t - actET_t - Q_t + \Delta TWS_t} \quad \text{(S21)}$$

with the change of total water storage ΔTWS [mm d^{-1}] resulting from

$$\mathbf{\Delta TWS = (SWE_t - SWE_{t-1}) + (SM_t - SM_{t-1}) + W_t} \quad \text{(S22)}$$

so that solving Eq.(S21) and Eq.(S22)

$$\mathbf{\Delta RW_t = actET_t + Q_t - P_t - (SWE_t - SWE_{t-1}) - (SM_t - SM_{t-1})} \quad \text{(S23)}$$

The amount of retained water RW [mm] at time t then results from

$$\mathbf{RW_t = RW_{t-1} + \Delta RW_t} \quad \text{(S24)}$$

Finally, the integrated terrestrial water storage TWS [mm] at time t represents the sum of all storage components:

$$\mathbf{TWS_t = SWE_t + SM_t + RW_t} \quad \text{(S25)}$$

S2 Uncertainty of the observational constraints

Maps of the temporal average uncertainties of observed TWS, ET and Q that are used for model calibration are shown in Fig. S1. For observed SWE a constant average uncertainty of 35 mm is applied.

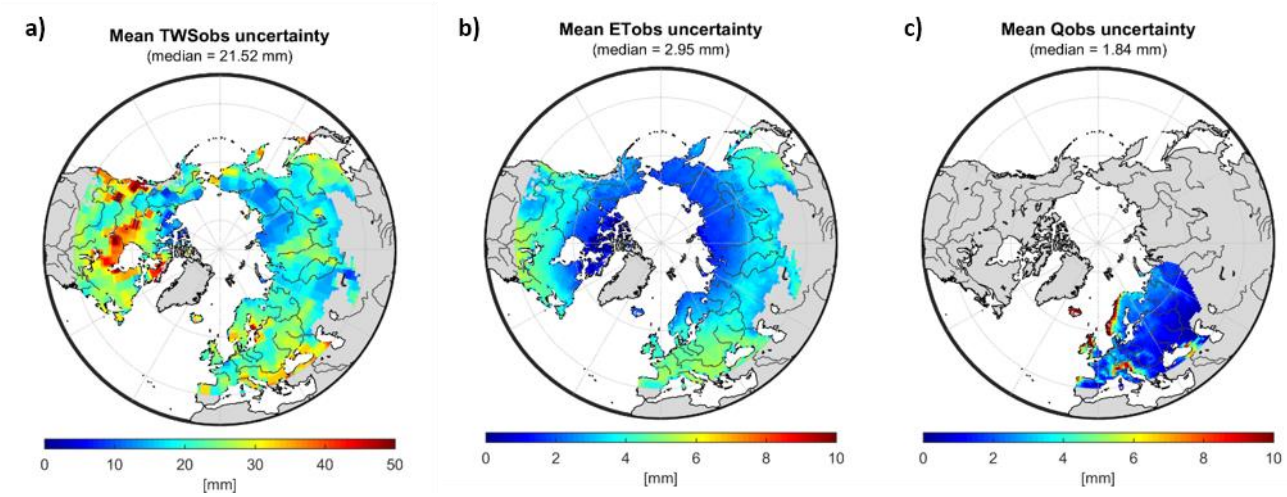

Figure S1. Mean uncertainty of monthly TWSobs [mm], and of the mean seasonal cycle of ETobs [mm d^{-1}] and Qobs [mm d^{-1}] used for model calibration. Values are truncated to 50 mm resp. 10 mm.

S3 Cost terms

Table S1 shows the cost terms achieved with the default and the optimized parameter set. Compared to the default parameter values, total costs clearly improve after calibration. The shown optimized values represent a weighted Nash-Sutcliff efficiency of 0.37 (TWS), 0.44 (SWE), 0.57 (Q) and 0.80 (ET) (weighted Nash-Sutcliff = 1 – cost value).

Table S1. Cost values obtained with the default and the optimized model parameters using Eq. (1).

parameter values	TWS	SWE	ET	Q	total
default	0.84	0.54	0.15	1.00	2.55
optimized	0.63	0.56	0.20	0.43	1.82

S4 Model performance regarding evapotranspiration and runoff

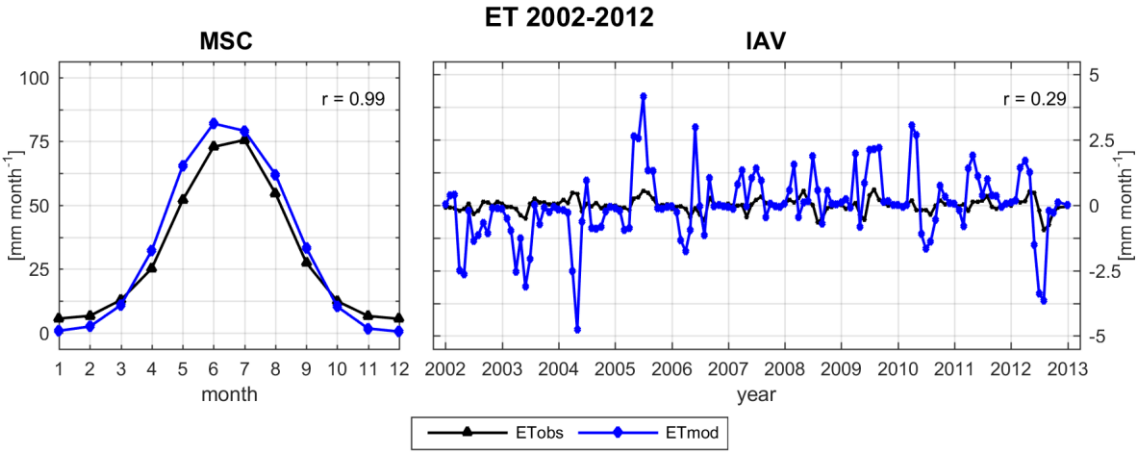

Figure S2. Spatially averaged mean seasonal cycle (MSC) of the period 2002–2012 and inter-annual variability (IAV, difference between monthly values and the MSC) for ETmod and FLUXCOM based ETobs.

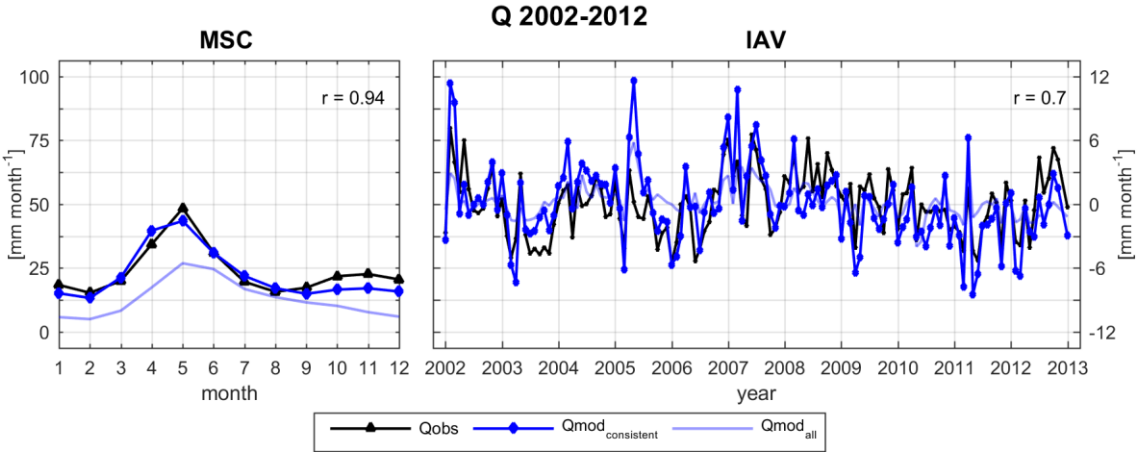

Figure S3. Spatially averaged mean seasonal cycle (MSC) of the period 2002–2012 and inter-annual variability (IAV, difference between monthly values and the MSC) for Qmod and EU-grid runoff Qobs. $Qmod_{consistent}$ solely considers grid cells that coincide with Qobs, while $Qmod_{all}$ is based on modelled runoff for all grids of the study domain.

5

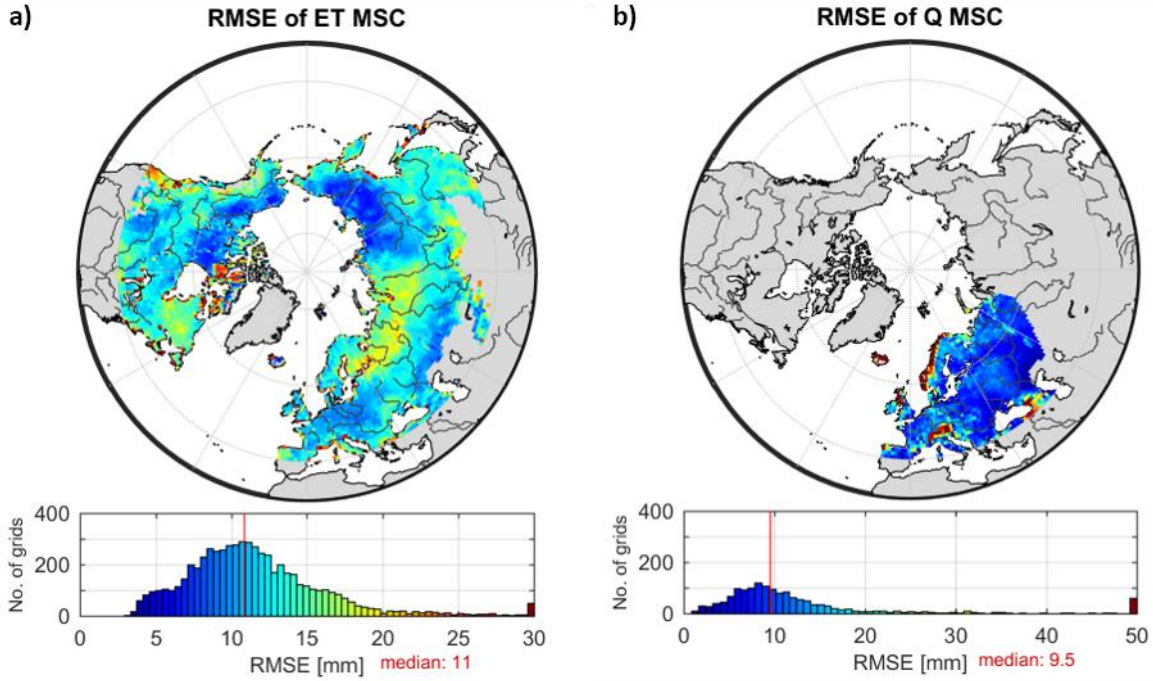

Figure S4. RMSE of the mean seasonal cycle of simulated and observed a) ET [mm $month^{-1}$] and b) Q [mm $month^{-1}$]. RMSE values have been truncated to the range 0–30 (a) resp. 0-50 (b).

S5 Phase shift in mean seasonal TWS

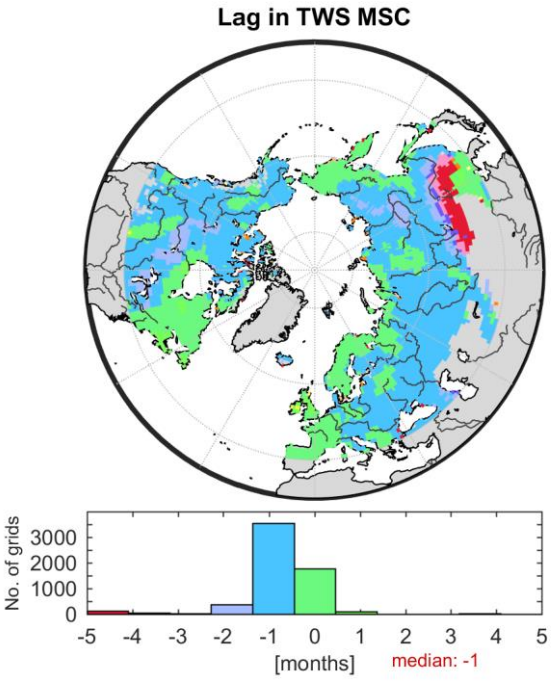

Figure S5. Grid wise phase lag [months] between mean seasonal TWSobs and TWSmod. Negative values indicate preceding of the model compared to GRACE TWS.

S6 Comparison with eartH2Observe models

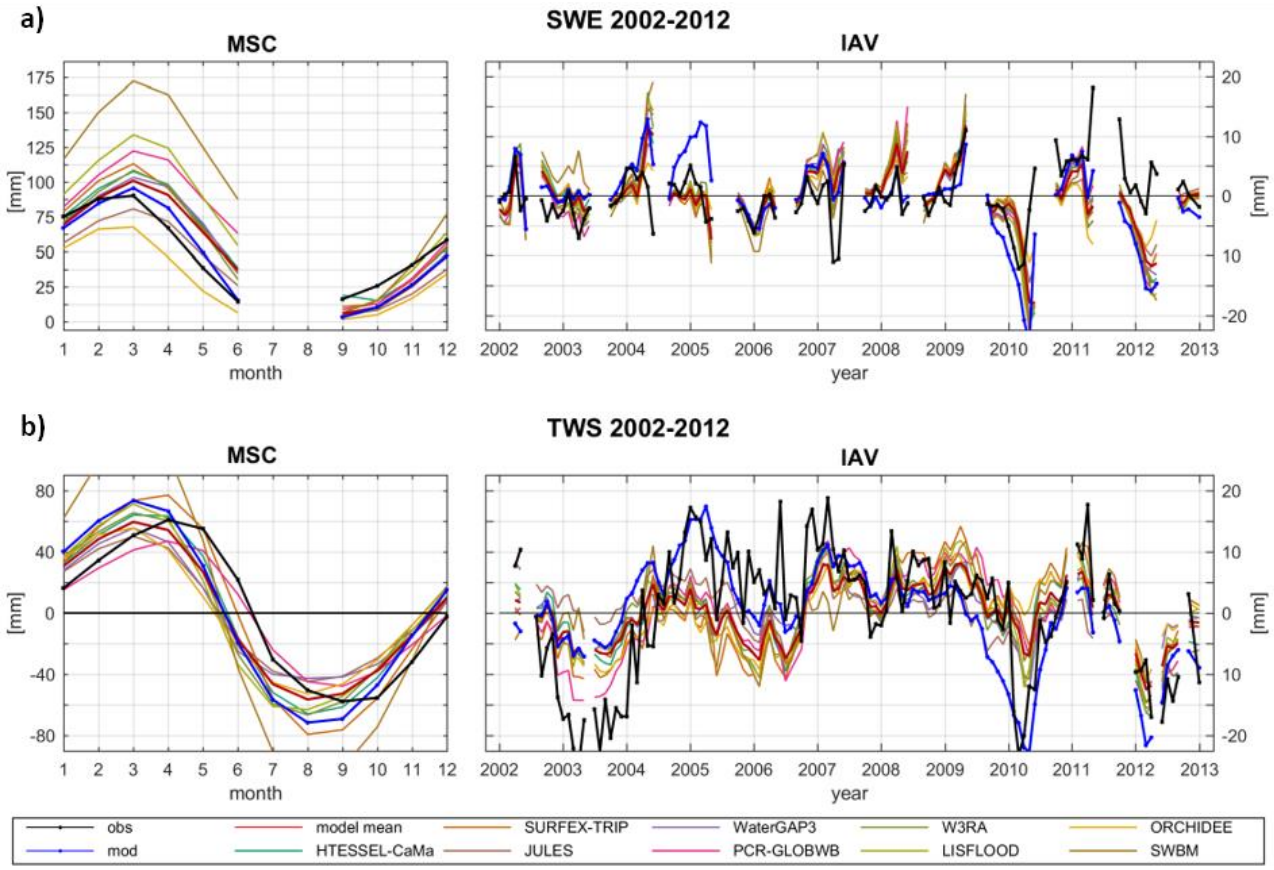

Figure S6. Comparison of spatially averaged observed (obs) **a)** SWE (GlobSnow) and **b)** TWS (GRACE) to simulations of this study (mod) and eartH2Observe models (incl. ensemble mean) in terms of average mean seasonal cycle (MSC) and inter-annual variability (IAV). MSC is calculated for the period 2002–2012, and IAV represents the difference of monthly values from the MSC. Only data points consistent between all models and the respective observational data are considered.

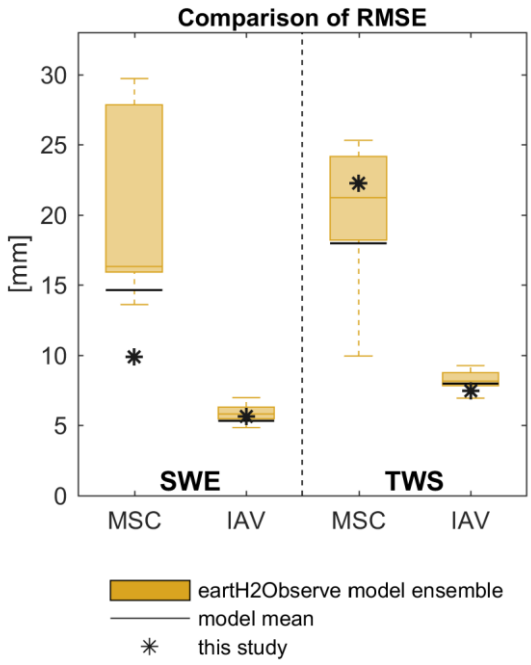

Figure S7. RMSE for the spatially averaged SWE (left) and TWS (right) achieved by our model compared to the model ensemble of eartH2Observe models and the ensemble mean across temporal scales.

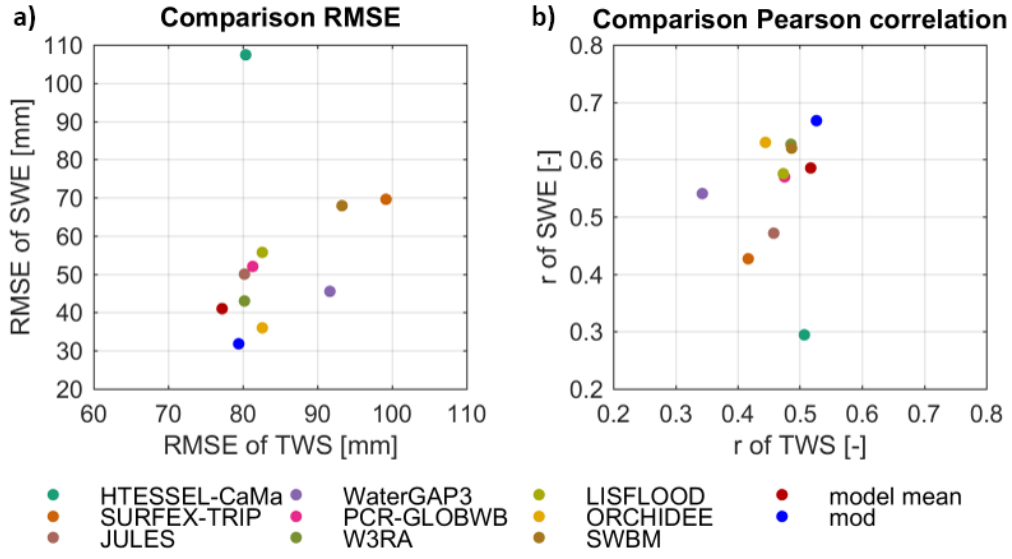

Figure S8. Comparison of a) RMSE and b) Pearson correlation r for monthly SWE and TWS time series simulated with the eartH2Observe models, the model ensemble mean (model mean) and by our model (mod).

S7 Uncertainty due to forcing and calibration data

S7.1 Comparison to WFDEI precipitation forcing

To assess the uncertainty in TWSmod and SWEmod that emerges from the choice of precipitation forcing, we calibrated our model in the same manner as before, yet used rain fall and snow fall estimates from the reanalysis based WFDEI product (Weedon et al. 2014) instead of GPCP-1DD precipitation data. Since precipitation is likely the most uncertain input data (Herold et al. 2015, Schellekens et al. 2017), we did not change the temperature and net radiation data sets. The global meteorological WFDEI data for land area is generated by applying the Water and Global Change (WATCH) forcing data methodology to ERA-Interim reanalysis data (Dee et al. 2011). The advantage of the WFDEI product is that it already provides separate values for snow and rain fall, as diagnosed by the reanalysis (Weedon et al. 2014). Therefore, it is not necessary to partition precipitation based on a temperature threshold within the model. We rather applied the provided rain and snow fall estimates directly, and also desisted from scaling snow fall.

Regarding the MSC, we obtained similar model performance in terms of SWE and TWS for both, the spatially averaged dynamics (Fig. S9, Fig. S10) and the spatial pattern (not shown). Although the dynamics and thus the correlation coincidence, we obtain a higher amplitude in TWSmod when using WFDEI as forcing compared to the original TWSmod (and TWSobs). This higher amplitude relates to larger seasonal snow accumulation in $SWEmod_{WFDEI}$, because the scaling parameter for snow fall is not calibrated. In terms of IAV, the correlation between observation and WFDEI forced model is comparable for both, TWS and SWE. However, the key findings (Fig. S11) remain the same as with GPCP precipitation forcing.

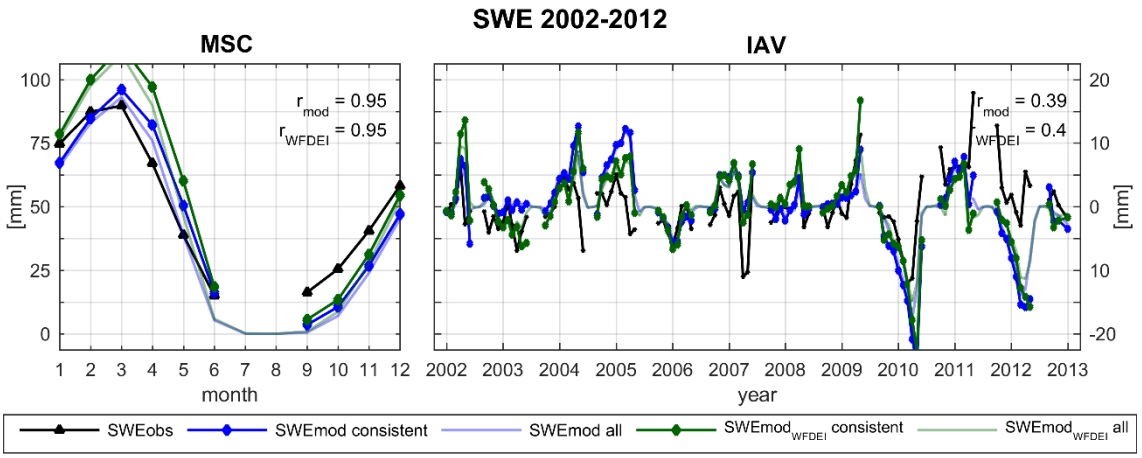

Figure S9. Comparison of the spatially averaged mean seasonal cycle (MSC) and inter-annual variability (IAV, difference between monthly values and the MSC) of observed SWE (SWEobs), modelled SWE (SWEmod), and modelled SWE based on WFDEI precipitation forcing ($SWEmod_{WFDEI}$). SWEmod consistent and $SWEmod_{WFDEI}$ consistent refers to modelled SWE considering only data points with available SWEobs, while SWEmod all and $SWEmod_{WFDEI}$ all incorporates all time steps for all grids of the study domain.

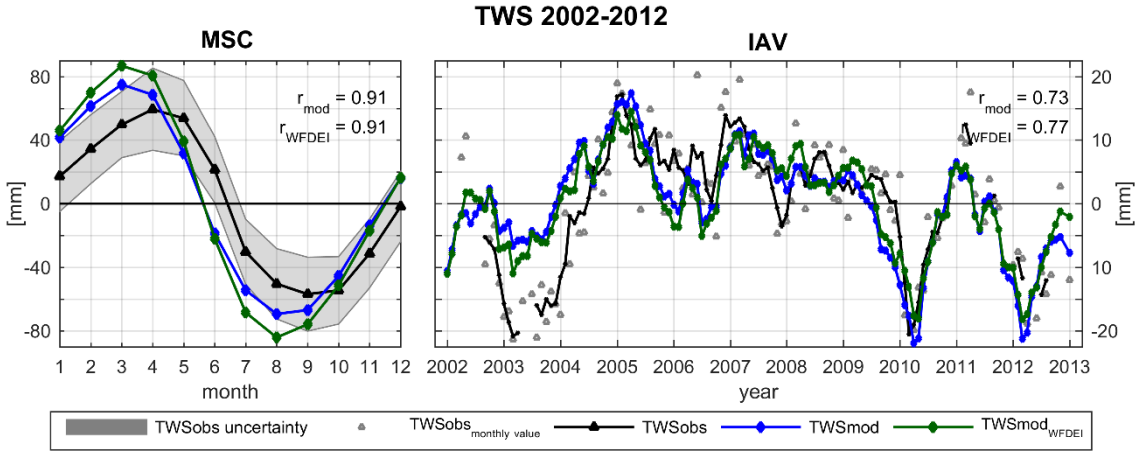

Figure S10. Comparison of the spatially averaged mean seasonal cycle (MSC) and inter-annual variability (IAV, difference between monthly values and the MSC) of observed TWS (TWSobs), modelled TWS (TWSmod), and modelled TWS based on WFDEI precipitation forcing ($TWSmod_{WFDEI}$). For IAV, $TWSobs_{monthly\ value}$ shows the original IAV of individual TWSobs months, while TWSobs, TWSmod and $TWSmod_{WFDEI}$ are smoothed using a 3-month average moving window filter. Pearson correlation r refers to the smoothed values. For the MSC no smoothing is applied.

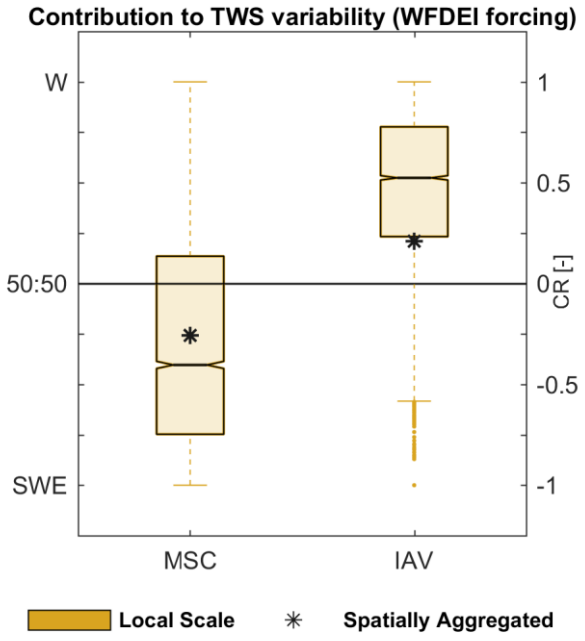

Figure S11. Relative contribution (based on CR (Eq.**Fehler! Verweisquelle konnte nicht gefunden werden.**))) of snow (SWE) and liquid water (W) to TWS variability on different spatial (local grid scale, spatially integrated) and temporal (mean seasonal MSC, inter-annual IAV) scales when forced with WFDEI rain and snow fall. The boxplots represent the distribution of grid cell CR, with the dashed line marking the corresponding average. The star represents the CR calculated for the spatially integrated values.

S7.2 Comparison to other GRACE solutions

In this study we used TWS estimates from the JPL mascon RL05 product for model calibration and evaluation (Watkins et al., 2015;Wiese, 2015). However, various GRACE solutions for TWS from different institutions and using different processing approaches exist. To assess the potential uncertainty resulting from the choice of TWS solution, we compared modelled TWS (mod) and the JPL mascon solution (JPL_{masc}) with other solutions based on different processing approaches. They include the mascon product from the Center of Space Research (CSR at the University of Texas) (CSR_{masc}) (Save et al., 2016), as well as three RL05 solutions based on spherical harmonics provided by JPL, CSR and GeoforschungsZentrum (GFZ) (Swenson and Wahr, 2006;Landerer and Swenson, 2012;Swenson, 2012). As recommended, we also considered the average of the latter three ($Avg_{JPL/CSR/GFZ}$). All TWS estimates were taken as anomalies to the respective time-mean of 2002–2012, and scaled with the provided gain factors (except for CSR_{masc} that does not require scaling (Save et al., 2016). For comparison, we calculated the spatial average mean seasonal cycle (MSC) and inter-annual variability (IAV) across all grid cells of the study domain (Fig. S12).

Thereby, we find that the spatial average MSC of all GRACE TWS estimates agrees in its dynamics, albeit minor differences in the solutions' amplitudes exist (by ±15 mm). This results in comparable correlation and RMSE with modelled TWS. As the signal itself is noisier on IAV scales, the GRACE solutions show broader variability for IAV than at MSC scales as well. However, the qualitative pattern between the solutions remains, and modelled TWS is not closer to one specific solution or another during the entire time period. Therefore, the uncertainty evolving from the choice of GRACE solution used for model calibration can be assumed to be minor.

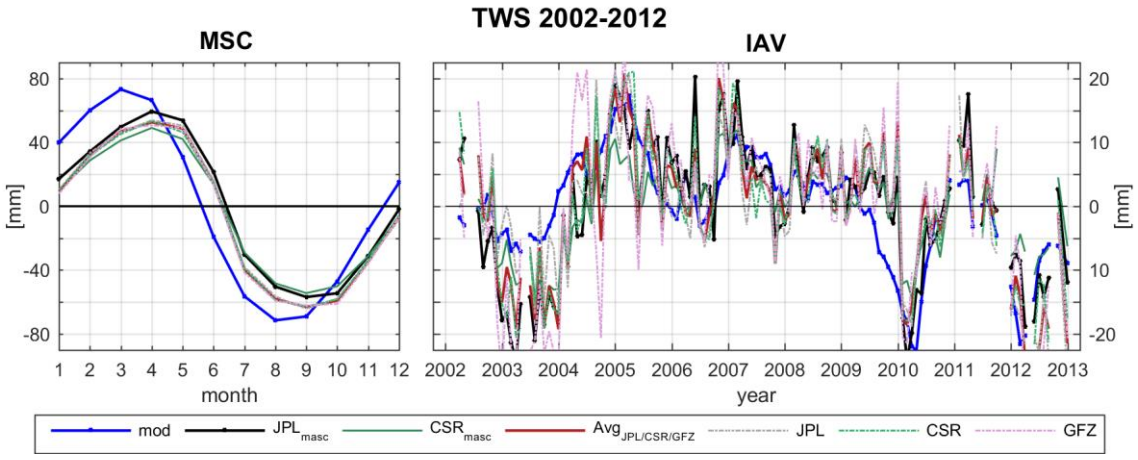

Figure S12. Comparison of the spatially averaged mean seasonal cycle (MSC) and inter-annual variability (IAV, difference between monthly values and the MSC) of modelled TWS (mod) and observed TWS of different GRACE solutions.

S8 Covariances between SWE and W

Figure S13 and Fig. S14 compare the contribution of the combined SWE and W variances and the covariance of both storages to the total variance of the spatially aggregated TWSmod. On the interannual and spatially aggregated scale, 81 % of TWS variability is explained by the variances in SWE and W, suggesting that the covariance between SWE and W only has minor effect. This is underlined by high percentage of SWE and W variance on total TWSmod variance for all grids of the study domain (Fig. S14). On mean seasonal scales, the majority of spatially aggregated TWS variability is still explained by variances in SWE and W, but the contribution of the covariance increases. This can be expected, as the seasonal variation of snow storage affects the subsequent availability of liquid water storages through the snowmelt process. At the local scale, though, the percentage of SWE and W variance on total TWSmod variance remains high in regions where the dominance of either snow or liquid water components are clear (Fig. 7 of the manuscript). In regions where covariances of two storage components is larger, the contribution of two storage components to TWS variability are similar resulting in a CR value of around 0. Therefore, we conclude that while the covariances of snow and liquid water can be remarkable on the seasonal scale over a large spatial domain, it does not affect or change the dominant components on the TWS.

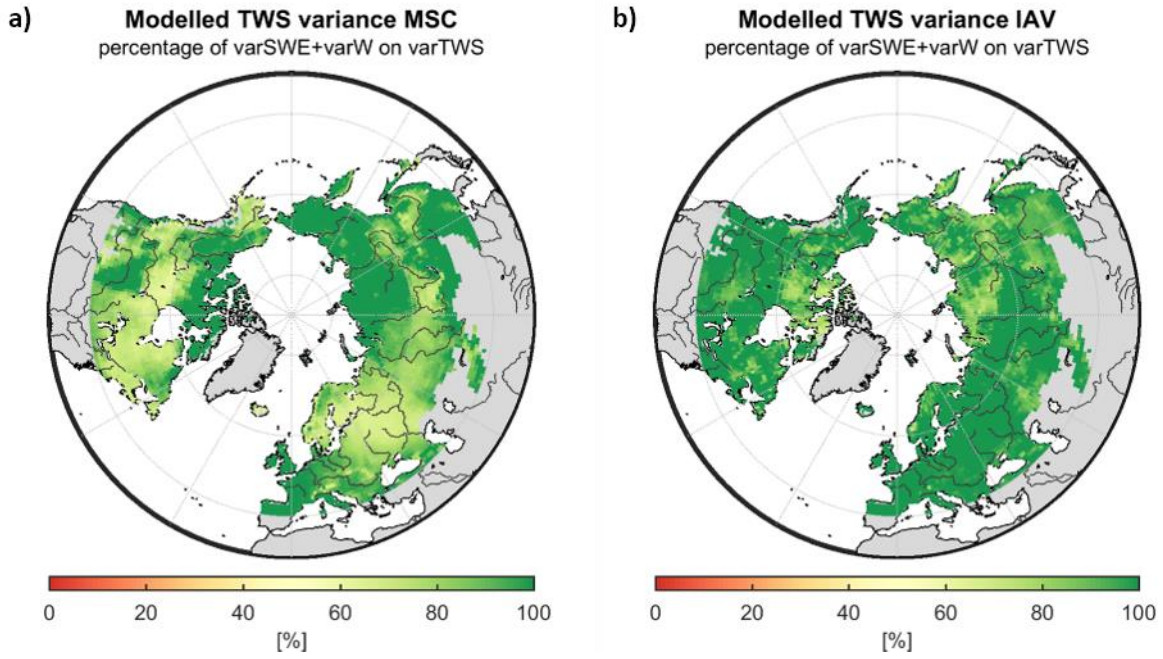

Figure S13. Percentage of SWE and W variance on total TWSmod variance on mean seasonal (MSC) and interannual (IAV) scales.

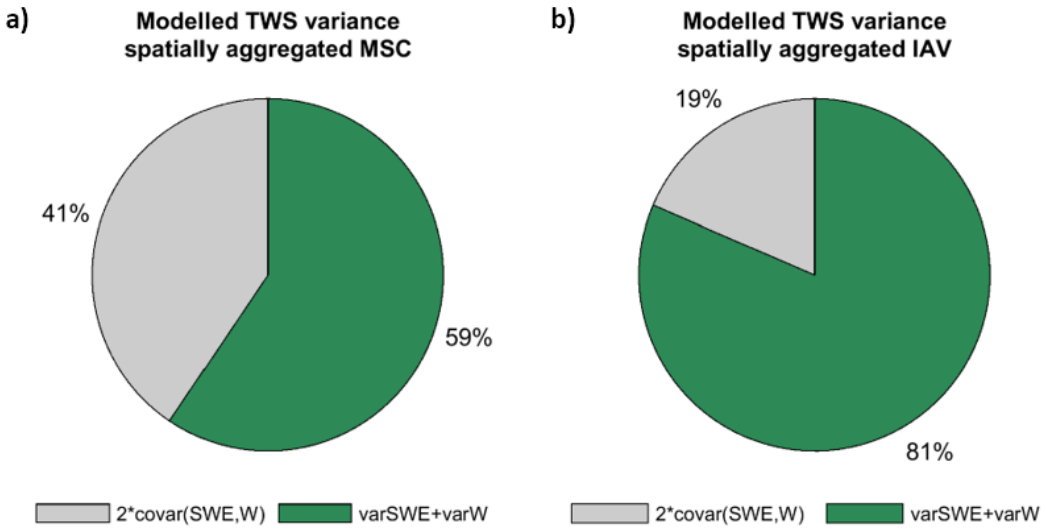

Figure S14. Percentage composition of spatially aggregated TWSmod variance from the combined variances of SWE and W, and two times the covariance of SWE and W on mean seasonal (MSC) and interannual (IAV) scales.

References

Balsamo, G., Beljaars, A., Scipal, K., Viterbo, P., van den Hurk, B., Hirschi, M., and Betts, A. K.: A Revised Hydrology for the ECMWF Model: Verification from Field Site to Terrestrial Water Storage and Impact in the Integrated Forecast System, Journal of Hydrometeorology, 10, 623-643, 10.1175/2008jhm1068.1, 2009.

Bergström, S.: The HBV model, in: Computer models of watershed hydrology., edited by: Singh, V., 443-476, 1995.

ECMWF: IFS Documentation - Cy40r1: Part IV: Physical Processes, in, European Centre for Medium-Range Weather Forecasts, Reading, England, 2014.

Kustas, W. P., Rango, A., and Uijlenhoet, R.: A simple energy budget algorithm for the snowmelt runoff model, Water Resources Research, 30, 1515-1527, 1994.

Landerer, F. W., and Swenson, S. C.: Accuracy of scaled GRACE terrestrial water storage estimates, Water Resources Research, 48, 10.1029/2011wr011453, 2012.

Miralles, D., Holmes, T., De Jeu, R., Gash, J., Meesters, A., and Dolman, A.: Global land-surface evaporation estimated from satellite-based observations, Hydrology and Earth System Sciences, 15, 453-469, 2011.

Murphy, D., and Koop, T.: Review of the vapour pressures of ice and supercooled water for atmospheric applications, Quarterly Journal of the Royal Meteorological Society, 131, 1539-1565, 2005.

Orth, R., Koster, R. D., and Seneviratne, S. I.: Inferring soil moisture memory from streamflow observations using a simple water balance model, Journal of Hydrometeorology, 14, 1773-1790, 2013.

Priestley, C., and Taylor, R.: On the assessment of surface heat flux and evaporation using large-scale parameters, Monthly Weather Review, 100, 81-92, 1972.

Rudolf, B., and Rubel, F.: Global Precipitation, in: Observed Global Climate edited by: Hantel, M., Geophysics Springer, Berlin, 567, 2005.

Save, H., Bettadpur, S., and Tapley, B. D.: High-resolution CSR GRACE RL05 mascons, Journal of Geophysical Research: Solid Earth, 121, 7547-7569, 10.1002/2016jb013007, 2016.

Seo, K. W., Ryu, D., Kim, B. M., Waliser, D. E., Tian, B., and Eom, J.: GRACE and AMSR-E-based estimates of winter season solid precipitation accumulation in the Arctic drainage region, Journal of Geophysical Research: Atmospheres, 115, 2010.

Swenson, S., and Wahr, J.: Post-processing removal of correlated errors in GRACE data, Geophysical Research Letters, 33, 10.1029/2005gl025285, 2006.

Swenson, S.: GRACE monthly land water mass grids NETCDF RELEASE 5.0 CA, USA, http://dx.doi.org/10.5067/TELND-NC005, 2012.

Teuling, A. J., Seneviratne, S. I., Williams, C., and Troch, P. A.: Observed timescales of evapotranspiration response to soil moisture, Geophysical Research Letters, 33, 10.1029/2006gl028178, 2006.

Watkins, M. M., Wiese, D. N., Yuan, D. N., Boening, C., and Landerer, F. W.: Improved methods for observing Earth's time variable mass distribution with GRACE using spherical cap mascons, Journal of Geophysical Research, 120, 2648-2671, 2015.

Wiese, D. N.: GRACE monthly global water mass grids NETCDF RELEASE 5.0 Ver. 5.0 Mascon Ver. 2, PO.DAAC, CA, USA, 2015.